

Article

Investigation on Key Parameters in the Fabrication of Stamps for Transfer Printing of Micro Devices

Changwen Su, Yue Lin, Tien-Mo Shih, Hao Lu, Yang Gao, Jia-En Huang, Yi-Jun Lu, Tingzhu Wu , Zhong Chen and Weijie Guo * 

Fujian Engineering Research Center for Solid-State Lighting, Collaborative Innovation Center for Optoelectronic Semiconductors and Efficient Devices, Department of Electronic Science, Xiamen University, Xiamen 361005, China; 33320171152749@stu.xmu.edu.cn (C.S.); yue.lin@xmu.edu.cn (Y.L.); tienmoshih@gmail.com (T.-M.S.); 33320171152759@stu.xmu.edu.cn (H.L.); yggao@stu.xmu.edu.cn (Y.G.); jehuang@stu.xmu.edu.cn (J.-E.H.); yjlu@xmu.edu.cn (Y.-J.L.); wutingzhu@xmu.edu.cn (T.W.); chenz@xmu.edu.cn (Z.C.)

* Correspondence: wjguo@stu.xmu.edu.cn

Received: 1 June 2020; Accepted: 28 June 2020; Published: 2 July 2020



Abstract: For the past few years, the transfer printing method has been developed and has secured numerous advantages. Here, via both experiments and analyses, we have focused on identifying key parameters and optimizing their values in the fabrication process of stamps for transfer-printing micro-devices. Specifically, the elastic modulus of posts is measured using the atomic force microscope and the Derjaguin, Muller, and Toporov model. Based on mold morphologies data, we subsequently explore the law of photoresist development under different design widths as well as development time, establish mathematical models, and offer relevant explanations for the formation of various developmental topographies. Furthermore, the relationship between the elastic modulus and these stamp-fabrication parameters has also been analyzed and confirmed. Hopefully, the proposed work can provide the guidance for fabricating reliable stamps in the future.

Keywords: AFM; DMT model; elastic modulus; lithography; PDMS stamps; transfer printing

1. Introduction

As a massively parallel assembly method, the transfer printing adopts a stamp to assemble diverse micron-nanoscale devices and materials, e.g., membranes, platelets, wires among others, into a two- or three-dimensional layouts [1,2]. It also qualifies as a highly versatile technique for heterogeneous integration on both rigid and flexible substrates [3], such as transferring concentrator photovoltaic cells [4], lasers [5,6], silicon micro-ICs [7], GaN LEDs [8], p-n junctions [9], and quantum dots [10]. This technology can also be used to transfer highly non-planar, globular structures, such as silica microspheres and grains of pollen [11] with high accuracy, high yield of 99%, and stamp life time of 200 h [12,13]. In general, researchers use viscoelastic polydimethylsiloxane (PDMS) as the stamp which, due to the softness of PDMS [14], can handle fragile materials without damages. In terms of procedure steps, the whole transfer printing process consists of (a) aligning and contacting the elastic stamp with devices on the donor substrate, (b) peeling off the stamp at a faster speed, and devices will be attached to the stamp by van der Waals force, (c) moving the inked stamp to the receiver substrate, and (d) peeling off the stamp at a lower speed. Afterwards, devices will be successfully printed on the receiver substrate [15].

Advantages of the transfer printing technology include: semiconductor devices can be transferred at the room temperature instead of at higher temperatures; the controllable, repeatable, and efficient transfer processes are expected to attain highly precise and large-scale rapid integration of

heterogeneous material arrays; and the natural transparency of the stamp enables the entire process to be observed through the stamp such that posts and devices-to-be-transferred can be precisely aligned. Incidentally, to make a sacrificial layer in a safer and more economical way, Nam et al. anneals the crucible at high temperatures to produce cerium oxide which can be used as a water-soluble sacrificial layer [16]. Striving for higher yield, Delamarche et al. suggest that the aspect ratio (height/width) of the post should lie between 0.5 and 5. At inappropriately low aspect ratios, the post cannot withstand the pressure during the transfer process, whereas, at overly high aspect ratios, the post tends to collapse during the transfer process [17].

Based on the method described above, there exists a surface relief assisted transfer method including micro tips [18] and gecko principle [19]: A stamp with a suitable surface relief structure enables adhesion control during retrieving and printing. Other transfer printing methods abound: load-enhanced transfer printing [20], laser-driven transfer printing [21,22], transfer printing based on shape memory polymer [23], overlay-aligned roll-transfer printing [24], fluidic assembly method [25], electrostatic adsorption, and electromagnetic force adsorption [26].

Transfer printing features a wide range of applications, including micro-LED display technology. Micro-LED display technology refers to the integration of high-density and micro-sized LED arrays on a single chip [27,28], with the size of the micro-LED $<100\ \mu\text{m}$ [29,30]. Generally, the traditional LED display endures a larger pixel size and a relatively poor display effect, whereas the micro-LED display has secured advantages of high resolution, high efficiency, high brightness, small size, more energy saving, and self-illumination without the need for a backlight [31,32]. In addition, key technologies of micro-LED display include bonding, current drive control, detection, and repair among others. As an essential step to the mass production of micro-LED display, the mass transfer of micro-LEDs constitutes the bottleneck of the full-colored micro-LED display technology.

As one of the important performances of the stamp for transfer printing, the elastic modulus exhibits the ability of stamp to resist elastic deformation under external forces. The adhesion force between the stamp and devices, originating from van der Waals force, can overcome the fact that, between devices and their carrier substrate, devices can then be successfully picked up by the stamp. Therefore, for the purpose of achieving the required adhesion force and picking up devices, it is necessary to press the stamp onto devices to squeeze out the air between the surface of the stamp and devices to ensure the effective contact between them. In cases of small elastic modulus of the stamp, the stamp will be severely deformed during picking up, deteriorating the yield of transfer printing. Therefore, it is of great significance to investigate the elastic modulus of fabricated stamps [33].

Some researchers have pioneered their work by employing casting and curing method to fabricate PDMS stamps. Kim et al. [18] report a unique adhesive surface for deterministic assembly of solid micro/nanoscale parts into two- and three-dimensional configurations. Lee et al. [34] demonstrate a method for integrating 2D/3D metamaterials/metadevices via the 3D modular assembly of each distinct meta-atom building block using an advanced mode of transfer printing. Ahmed et al. [35,36] present a novel composite stamp design for transfer printing and demonstrate the ability to print with cantilevered stamps. Yang et al. [37] demonstrate that adhesion switchability associated with angled features of relief in elastomer stamps for transfer printing offers new modes of high efficiency operation compared to previously reported cases.

Differently here, we place the emphasis on analyzing parameters that affect the size of the stamp, the mold, and the elastic modulus of the stamp. Furthermore, we describe fabrication processes in detail and challenge difficulties of the problem. We study the average deviation between the width of the post and the design width and state reasons for the deviation. Different types of morphologies of the photoresist mold during the development and reasons for the formation of different morphologies are summarized. We also study the law of development and establish mathematical models which provide criteria for determining fabricating parametric values based on target stamp specifications. The consequence of analyses greatly helps researchers reduce the exploration time required for fabricating stamps.

2. Materials and Methods

2.1. Stamps Fabrication

The whole stamps fabrication processes were performed under the air conditions, 22 °C, and 45% RH environment. At first, the 2-inch silicon wafer (Ke-Jing Corp., Anhui, China) was boiled at 250 °C on the hot plate (HT-300, Gdana Corp., Guangdong, China) for 15 min using a piranha wet etch, 98% H₂SO₄ (Jihua Corp., Jiangsu, China): 30% H₂O₂ (Atofina Corp., Shanghai, China) = 4:1. Then, this boiling process was followed by a deionized water rinse, as shown in Figure 1a. After the silicon wafer was dried with nitrogen (Tongwei Corp., Xiamen, China), it was baked under 135 °C in an oven (ESPEC Corp., Shanghai, China) for 4 h. The wafer should be cooled to the room temperature before spin coating to reduce the effect of temperature on the photoresist. For the purpose of preventing the wafer from contamination, the spin coating was performed immediately after the cooling.

As shown in Figure 1b, for better uniformity, a type of negative photoresist (SU-8 2075, Micro-Chem Corp., Newton, MA, USA) was spun using a spin coater (EZ4, Analysis Corp., Hongkong, China) at 500 rpm for 12 s and then at 4000 rpm for 40 s with the ultima thickness of ~40 μm. Because of a wide range of spin coating thickness between 0.5 μm to 650 μm, the SU-8 photoresist was chosen. Kim et al. [18] used SU-8 50 photoresist; while we used SU-8 2075 photoresist, the thickness of which ranged from 40 μm to 240 μm.

After the photoresist was spin-coated, the edge bead removal should be conducted. This removal process not only reduced the contamination of the hot plate when baking, but also enhanced the distance between the silicon wafer and the mask (Qingyi Corp., Shenzhen, China) to obtain a better effect when exposure.

As shown in Figure 1c, the photoresist-coated silicon wafer was baked (soft bake) on the hot plate at 65 °C for 3 min and then at 95 °C for 9 min. Afterwards, the silicon wafer was removed from the hot plate, and was cooled to the room temperature. If the film was wrinkled, the wafer should be placed on the hot plate for a few more minutes. Heating and cooling processes should be repeated until the film did not wrinkle.

Lee et al. [34] also used lithography technology to fabricate stamps. In this article, a long pass filter (Chroma Corp., Vermont, VT, USA) was used to eliminate UV radiation below 350 nm such that the verticalness of pattern sidewalls can be enhanced during the exposure, as shown in Figure 1d. Notably, multiple sets of experiments were performed to achieve the best exposure dose. Finally, the photoresist was exposed under a lithography machine (Model 200, OAI Instruments, Milpitas, CA, USA) at the power of 250 W for 10 s. At unsuitably low exposure-dose levels, the exposed photoresist would have been insufficiently cured, resulting in the severe erosion of the pattern edge when the photoresist was developed.

As shown in Figure 1e, post exposure bake (PEB) should be carried out immediately after the exposure. In this step, the wafer was baked on the hot plate at 65 °C for 2 min and then at 95 °C for 10 min. If insufficient time was spent for PEB, edges of the photoresist pattern would also be eroded after the development. After 1 minute of PEB at 95 °C, the latent image would appear. Otherwise, the failure for the appearance of the latent image suggested insufficient exposure or heating. When PEB was finished, the temperature of the sample on the hot plate should be slowly lowered to the room temperature.

As shown in Figure 1f, when thicker or larger aspect-ratio structures were developed, strong agitation should be performed. In addition, an ultrasonic bath was recommended during developing fine patterns. In this experiment, the development was performed using the development solution (SU-8, Micro-Chem Corp., Newton, MA, USA) for 10 min and then an ultrasonic bath under 53 kHz in an ultrasonic cleaning machine (DTC-15J, Dingtai Corp., Hubei, China) for another 10 min. Incidentally, it was preferable to use containers which would not react with the developing solution, such as glass, during the development.

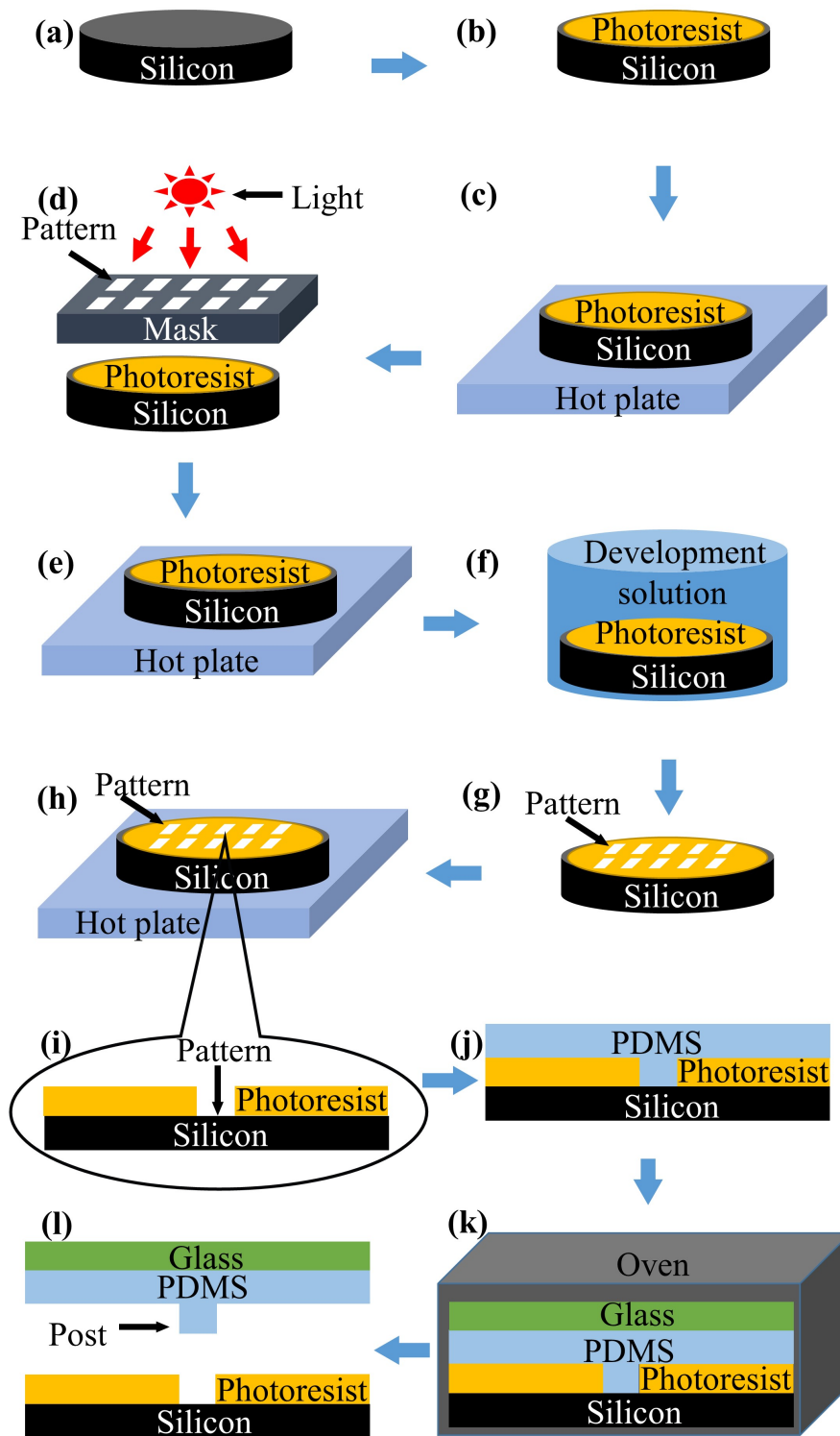


Figure 1. Schematic illustration of stamp fabrication processes (a) cleaning and drying; (b) spin coating; (c) soft bake; (d) exposure; (e) post exposure bake; (f) development; (g) rinsing and drying; (h) hard bake; (i) the cross section of the mold; (j) pouring PDMS; (k) curing; (l) peeling off.

After silicon-photoresist molds were developed in the development solution, they were rinsed with fresh development solution for 10 s and subsequently rinsed with isopropanol solution

(Qixiangtengda Corp., Shandong, China) for another 10 s, then silicon-photoresist molds were dried using a nitrogen gun as shown in Figure 1g. Yang et al. [37] also used lithography technology to fabricate stamps. Here, we used isopropanol solution to rinse off the residue on silicon-photoresist molds. If a white film appeared during the rinsing with isopropyl alcohol, this appearance indicated insufficient development. Under this circumstance, appropriate development operations should be performed, and were followed by the rinse and dry step.

Properties of SU-8 2000 photoresist would change after encountering higher temperatures. Therefore, the photoresist ought to be baked at a temperature of 10 °C higher than the ultima operating temperature, usually at 150 °C to 250 °C for 5 to 30 min (hard bake), as shown in Figure 1h. The hard bake step helped improve the photoresist surface cracking that occurred after the development. In this experiment, the soft bake was optimized as 3 min under 65 °C and as 9 min under 95 °C. Likewise, for a better exposure, the optimal dose was determined as 250 W for 10 s. The best time for PEB was determined as 2 min under 65 °C and 10 min under 95 °C.

After steps aforementioned, the stamp mold was completed. For the fabrication of stamps, the 184-silicone elastomer and the curing agent (Sylgard 184, Dow Corning Corp., Midland, MI, USA) were mixed in a ratio of 10 : 1 and were stirred evenly. After stirring, the mixture was placed in a vacuum chamber (SLZK-40, Shengli Corp., Shanghai, China) for 30 min, so that bubbles would escape. Then, the mixture (PDMS) was cast into the mold, and a piece of 2-inch glass (Fuyao Corp., Fujian, China) was covered on it as a carrier. Later, all of them were placed in the vacuum chamber (−72 cmHg) for 30 min again to remove bubbles and then were baked at 60 °C for 24 h, as shown in Figure 1j,k. When the PDMS was cured, it was peeled off from the mold and the PDMS was formed on the glass carrier, as shown in Figure 1l. Note that, during baking, samples should be placed in the oven after the temperature rose to the desired point to ensure that the PDMS was cured at the precise temperature. In addition, the more highly the temperature reaches, the more easily the silicon wafer would be broken, leading to the problem that stamps would not be easily peeled off.

Lee et al. also used casting and curing method to fabricate stamps, and they transferred PDMS patterns on the glass after the PDMS was cured [38]. However, prior to curing PDMS, we covered a piece of glass on PDMS; after PDMS was cured, it would be formed on the glass carrier directly. Fewer steps and less time in our method were required.

2.2. Characterization

For the purpose of measuring the width of posts and molds, the step profiler (Dektak-XT, Bruker Corp., Karlsruhe, Germany) was chosen. First, the sample was placed on the central of the stage of the step profiler. The stage was rotated to adjust the sample direction. Then, we lowered the probe to near the sample surface, as well as set (a) the size of the field of view, (b) the measurement length, and (c) the moving speed and pressure of the probe. Subsequently, we selected the starting point and started the measurement. Finally, we analyzed the measured data to obtain the width of the sample. For the same measurement point, we repeated the measurement process for 5 times and took the average value as the measurement result. For the sake of reducing the measurement error, it was forbidden to touch the step profiler during the whole measurement process. During the measurement process of the post width, the pressure and the movement of the probe would cause convex deformation to the post, leading to the measurement error, which could be eliminated by reducing both the pressure and the moving speed of the probe.

For the purpose of measuring the height/depth of posts and molds, the laser confocal microscope (OLS 5000, Olympus Corp., Tokyo, Japan) was chosen. First, the sample was placed on the central of the stage of the laser confocal microscope. The stage was rotated to adjust the sample direction. Then, the appropriate objective lens was selected and was lowered to near the sample surface. The objective lens would automatically focus by itself. Next, we selected the measurement area and set the size of the scanned field of view. Subsequently, we set the starting point, the ending point, the speed, and the accuracy of scanning and started measurements. Finally, we analyzed the measured

data to obtain the depth/width of the sample. For the same measurement point, we repeated the process five times and took the average value. For the sake of reducing the measurement error, it was forbidden to touch the laser confocal microscope during the whole measurement process.

For the purpose of measuring the elastic modulus of stamps, AFM (Atomic Force Microscopy, Cypher S, Asylum Research, Santa Barbara, CA, USA) was chosen. First, the elastic coefficient of the AFM cantilever was calibrated. Generally, the elastic coefficient of the AFM cantilever played an important role for the measurement of the elastic modulus. By contract, that of the cantilever provided by the manufacturer usually endured the shortcoming of a relatively large uncertainty and might deviate from the actual value. In avoiding errors caused by sample deformation during calibration, the sapphire (Crystal Technical Material Corp., Anhui, China), much harder than the tip, was used for calibration. In addition, for the sake of avoiding changes in sensitivity, it was prohibited to move the installation position of the cantilever and the laser spot during the entire calibration process. Second, the AFM cantilever was used to measure its force–displacement curve against the stamp, which was cut to a size of about 1 cm by 1 cm for measurements. After that, the stamp was glued to the metal sheet which was magnetically attracted to the AFM stage. Then, AFM's contact mode was selected, using a 20× objective lens and a probe of AC160TS-R3, with the depth inserted into the post of ~1 μm. Third, the force–displacement curve was fitted to the DMT (Derjaguin, Muller, and Toporov) model to obtain the value of the elastic modulus. Finally, five different points on the same sample were measured, and their average value was regarded as the elastic modulus of the sample.

3. Results and Discussion

3.1. Size Measurement

The height and the depth of posts and molds measured by the step profiler show more accurate results than the width measurement. Due to the taper nature of the probe used in the step profiler, the cross section of the probe in contact with the sample varies at different heights or depths. In addition, the diameter of this cross section equals the error in measuring the width of the sample. For measurements, the laser confocal microscope adopts an optical principle, which does not affect measured samples, resulting in higher measurement accuracy. Through measurements and analysis, we obtain that, for both top and bottom faces, the average error between the post's width and the mold's width can be controlled within 5%. Similarly, the standard deviation of the height of posts fabricated in the same batch can be controlled within 0.5 μm.

We study the average deviation between the width of the post and designed mask pattern width as shown in Figure 2f and conclude that the deviation value shows relatively stable regardless of the size. Because angles of light coming from different mask patterns appear relatively consistent during exposure. The overall average deviation of the top face is positive (16.84 μm), while that of the bottom face is negative (−3.23 μm). Due to the expansion of PDMS during curing, the deviation of the top face stays positive. Next, the deeper the photoresist mold becomes, the harder it is to ensure the verticality of the side wall during development, resulting in a negative deviation of the bottom face of the post.

In this set of experiments, sizes of fabricated posts range from 20 μm to 180 μm. The post should size closely to the chip, so that transfer printing can be better performed. Equally notably, for transferring flip chips, the top surface of the chip instead of PN pads (P-pad and N-pad of the LED chip) is attached to posts of the stamp. Therefore, flip chips with any PN gap value (the gap between P-pad and N-pad of the LED chip) can be adapted to posts. When the adhesion force between the post and the chip can overcome the force between the chip and its carrier substrate, the chip can be successfully picked up by the stamp.

Kim [18], Lee [34], Ahmed [35,36], and Yang [37] have pioneered their work by employing casting and curing method to fabricate cuboid-post stamps, the width of whose posts are over 100 μm; in comparison, our posts of stamps contain the widths from 20 μm to 180 μm. Furthermore, we

study the average error between the post's width and the mold's width. Filipponi [39] et al. fabricate pyramidal posts, while we fabricate cuboid posts. The average error between the post's width and the mold's width can be controlled within 5% both in their and our work.

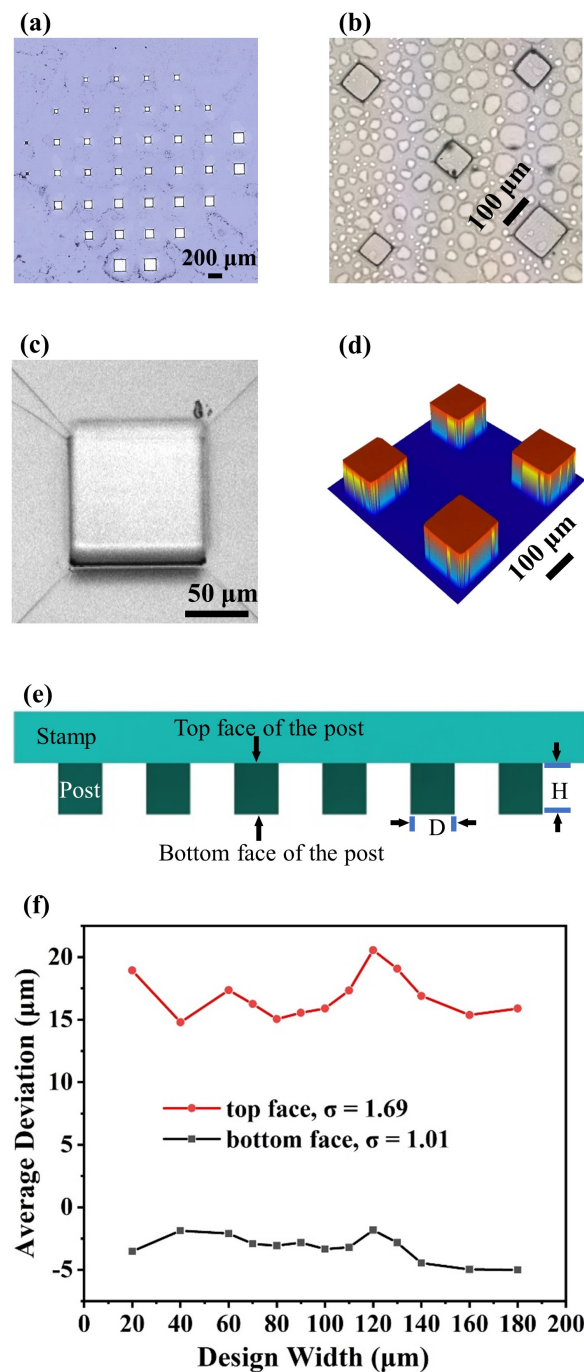


Figure 2. Fabricated molds and stamps as well as stamps' measurement results (a) fabricated molds under the optical microscope; (b) fabricated stamps according to the molds in Figure 2a under the laser confocal microscope; (c) enlarged view of the stamp in Figure 2b under the laser confocal microscope; (d) 3D image of posts in Figure 2b under the laser confocal microscope; (e) schematic illustration of a stamp; (f) average deviation between the width of the post and design width. Red dots represent the average deviation between the width of the top face of the post and designed width; black rectangles represent the average deviation between the width of the bottom face of the post and designed width.

3.2. Development Effect under Different Conditions

Figure 3a–e shows several types of morphologies of photoresist molds during the development process, including successful and failed ones. We apply semi-ellipsoid fitting to the successful morphologies as shown in Figure 3a,f and Equation (1) for the purpose of exploring development laws of the mold and providing the reference for subsequent researchers to fabricate molds and stamps.

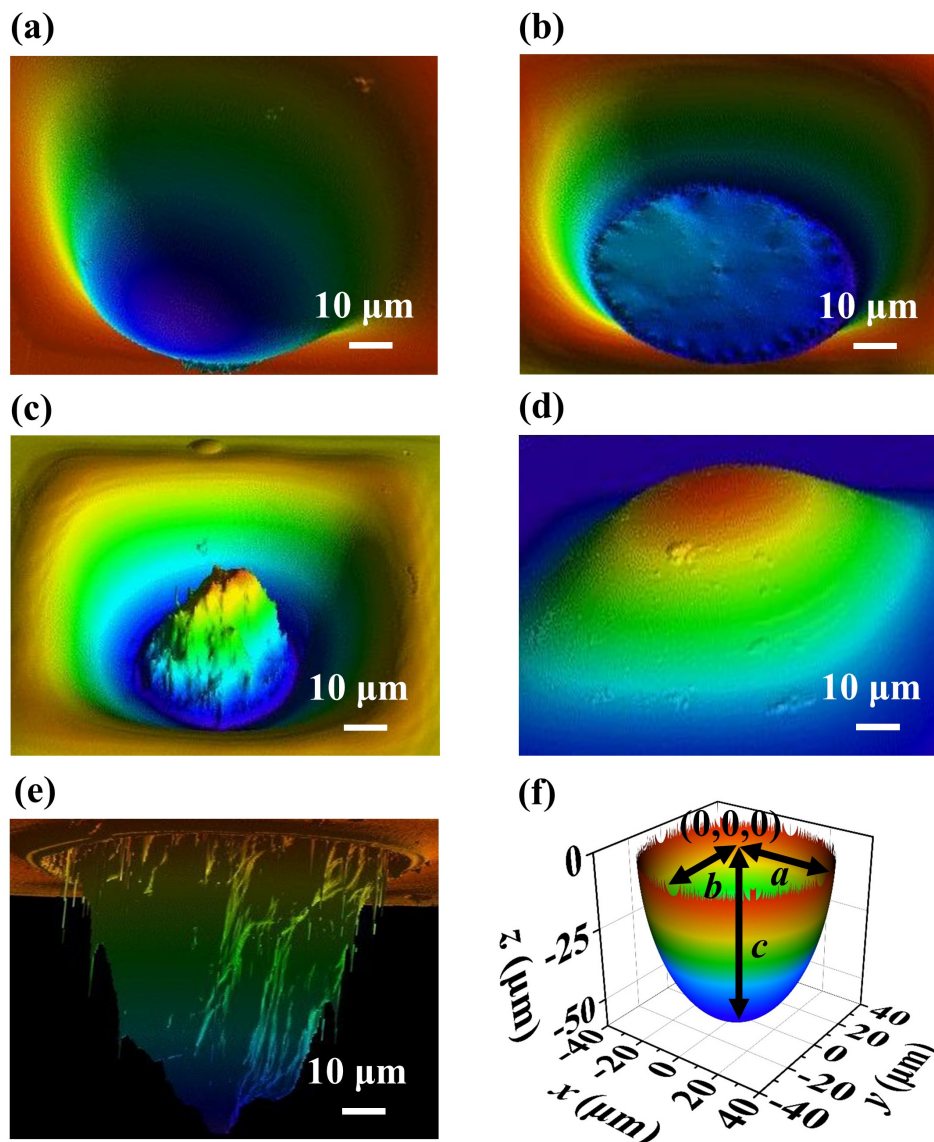


Figure 3. Several morphologies of molds during the development process, including successful and failed ones; (a–e) five different mold development morphologies under a laser confocal microscope (OLS 5000, Olympus Corp., Tokyo, Japan); (f) schematic illustration of a semi-ellipsoid.

After the photoresist has been developed, it remains in the exposed parts of the photoresist mask, as shown in Figure 2a. Figure 3 provides morphologies of the photoresist during the development. The photoresist in patterned parts on the silicon substrate is gradually removed over time. The morphologies of the mold fall into five categories, as illustrated in Figure 3. Among them, the semi-ellipsoidal shape illustrated in Figure 3a is of the majority. A variation of this kind is a truncated-cone, with a relative flat bottom, as shown in Figure 3b. Figure 3a shows the normal

morphology during the development, and Figure 3b shows the morphology that the photoresist is about to be completely removed.

Categories other than these two are considered as failures, as illustrated in Figure 3c,e, which show either a hill-like projection or a convex, or other irregular shapes. The morphology in Figure 3d is formed by the overflowed photoresist, and morphologies in Figure 3c,e can be attributed to uneven stirring during development.

Thus, we only focus on regular ones, namely, the semi-ellipsoidal shapes. Other remaining results cannot be processed satisfactorily. During the development process, the central area has been developed faster than the surrounding has, resulting in the depth > the radius. The difference in the developing speed can be attributed to (a) during exposure, the curing intensity on side walls of the mold appears greater than that on the bottom of the mold, and (b) the developer will accelerate the etching of the photoresist at the bottom of the mold due to the gravity. For analyses, we fit the semi-ellipsoidal part at the bottom of molds fabricated under different development conditions with the semi-ellipsoid equation

$$z = -c\sqrt{1 - \frac{x^2}{a^2} - \frac{y^2}{b^2}}, \quad (1)$$

where parameters a , b , and c represent the length of the three half axes of the semi-ellipsoid, respectively, as shown in Figure 3f. These data have been fitted with acceptable accuracies (average $R^2 = 0.93$). Due to isotropic etching of the lateral of the mold, we combine parameters a and b into one radius as

$$r = \frac{a + b}{2}. \quad (2)$$

During the development, since the etching speed at the bottom of the mold exceeds those of laterals, the value of c should surpass that of r . Therefore, we linearly fit values of c with r , as shown in Figure 4a and

$$c = -3.04 + 1.37r \quad (24.44 \leq r \leq 94.70, R^2 = 0.982), \quad (3)$$

showing a slope of 1.37—etching speed in the vertical direction reaches 1.37 times that in the lateral direction.

Primarily, the deviation between measurement dots and the fitting curve in Figure 4a originates from the deviation between morphologies of the developed mold and the semi-ellipsoid. Values of c and r are fitted from Figure 3, in which the shape of the mold during development is assumed to be semi-ellipsoidal shape. However, it is somewhat difficult for the actual shape of the mold during the development to precisely match the semi-ellipsoidal.

During the development process, both c and r are growing, whereas the growth is also infected by the setting width. We plot both c and r with the developing time duration t , at each setting width w , as shown in Figure 4b,c. As observed in the figure, multivariate linear fitting results, namely, in

$$r = -25.53 + 2.18t + 0.60w \quad (2 \leq t \leq 5, 80 \leq w \leq 180, R^2 = 0.97), \quad (4)$$

$$c = -46.43 + 5.40t + 0.80w \quad (2 \leq t \leq 5, 80 \leq w \leq 180, R^2 = 0.93), \quad (5)$$

conspicuously depict the linear relationship among r , c , and w . Slopes of 2.18 and 0.60 in Equation (4) indicate that, for each of increase in development time duration, and each of increase in designed width, values of r increase by an average of 2.18 and 0.60 μm , respectively, and so do slopes of 5.40 and 0.80 in Equation (5). At this juncture, a relationship between r , c , and w , t has been established. Next, the thickness of the photoresist fabricated in this set of experiments is approximated as 180 μm . If the thickness differs, the relationship among c , r , t and w may also differ slightly.

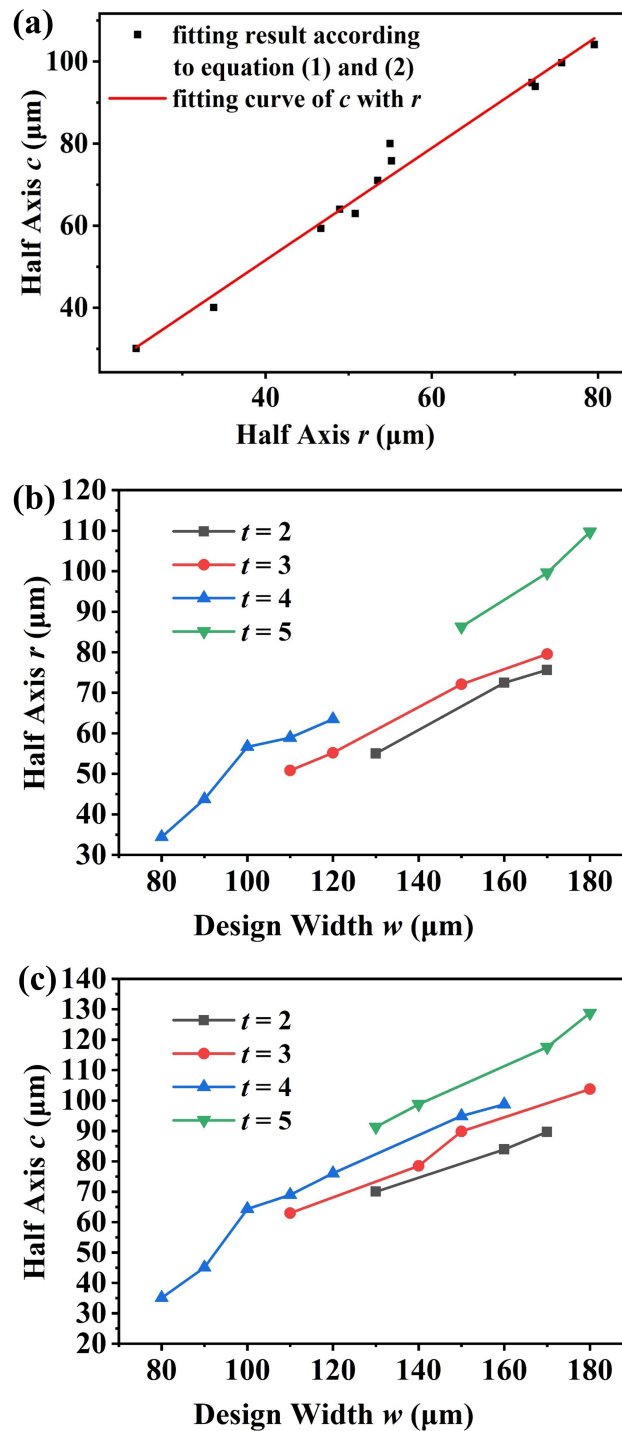


Figure 4. The relationship between the process parameters of the mold (a) results of a linear fit of c with r ; (b) the relationship among r and development time duration t , the designed width w of the mold; (c) the relationship among c and development time duration t , the designed width w of the mold.

3.3. Elastic Modulus Measurement

To measure the elastic modulus of posts, Bao et al. use AFM and the Hertz model [17]. In our study, the AFM and DMT model have been used instead, as shown by the inset in Figure 5a. Our rationale lies in the fact that the Hertz model suits measurements for the elastic modulus of a rigid sample,

whereas DMT does measurements for the elastic modulus of a viscous sample. Jiading et al. primarily study the effect of the temperature on the elastic modulus of PDMS. In addition, we also study the effect of the width on the elastic modulus [40].

Through AFM, we obtain the force–displacement curve of the cantilever with respect to the post during both inserting and retrieval processes. Then, we use the DMT model to fit the retrieval curve to acquire the value of the elastic modulus. The reason why we choose the retrieval curve instead of the inserting curve lies in the fact that, when the probe approaches the stamp, the atomic force between the probe and stamp will affect measurement results during inserting.

At the width of 130 μm , the elastic modulus reaches the maximum, as shown in Figure 5a. Figure 5b shows the elastic modulus of stamps with different curing temperatures. The elastic modulus of the stamp reaches the maximum of 25 Mpa and 38 Mpa at the curing temperature of 62 $^{\circ}\text{C}$ and 142 $^{\circ}\text{C}$, respectively. However, the elastic modulus of PDMS is related to the proportion of curing agent, curing temperature, curing time, and the precision of the measuring instrument. According to experimental results, within a certain range, the more the PDMS curing agent exists, the greater the elastic modulus becomes; the longer the curing time elapses, the greater the elastic modulus also becomes. Consequently, the deviation between measurement dots and the fitting curve may originate from the measuring deviation between different experiments and fitting deviation with the DMT model. The average measuring deviation between different experiments and fitting deviation with DMT model is ~ 3 Mpa (σ).

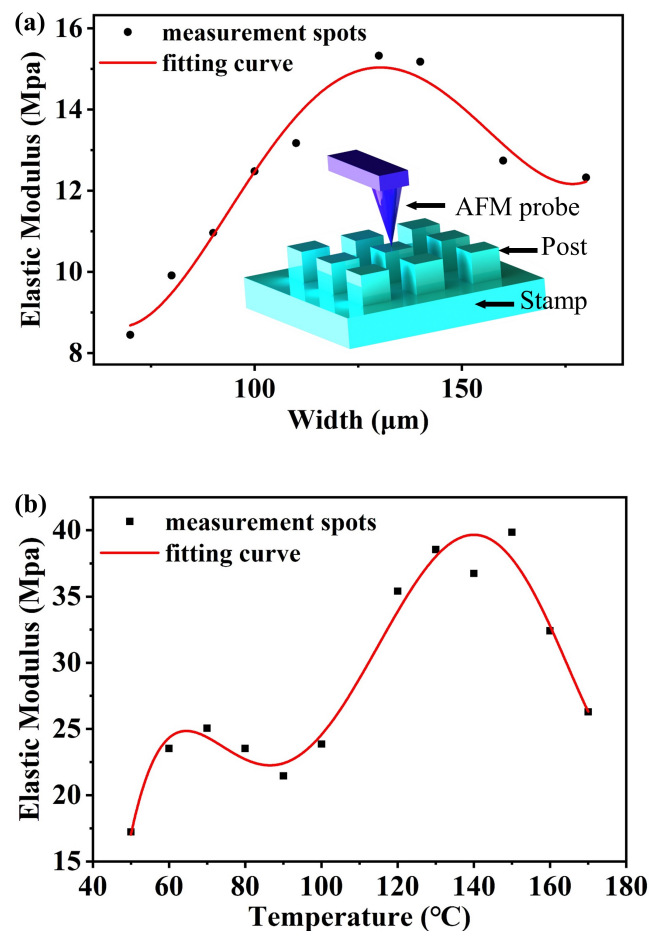


Figure 5. Elastic modulus measurement; (a) elastic modulus of posts with different widths (curing at 60 $^{\circ}\text{C}$, height: 46 μm , inset figure: an AFM-based method for measuring the elastic modulus of a post); (b) elastic modulus of posts with different curing temperatures (height: 46 μm , width: 130 μm).

We conduct transfer printing experiments of LEDs with stamps fabricated in our lab. Prior to the experiment, GaN-based flip-chip LEDs are supplied by Xiamen Changelight Co. Ltd., Xiamen, China. The LED wafer is grown on the sapphire substrate with InGaN/GaN multiple quantum wells and at the emission wavelength of 460 nm. In addition, flip-chip LED chips are fabricated and packaged by regular chip process with the size of $100 \times 200 \mu\text{m}^2$.

After several hundred times of transfer printing experiments, we have demonstrated that lab-made stamps have managed to transfer LEDs at a high yield. Incidentally, transfer printing experiments carried out using our stamps have been published as independent work [41].

Choi et al. [42] acquire the pressure and peeling speed of the stamp in the printing step, while we do the pressure and peeling speed of the stamp in the picking-up step. In our study, the best picking-up pressure ranges from 5 to 50 mN, and the best picking-up speed ranges from 17 to 21 mm/s.

The pressure and the peeling speed of the stamp in the picking up step in Kim et al.'s [18] study are 1 mN and 1 mm/s, respectively. The reason for differences between their pressure, peeling speed, and that of ours lies in the fact that they pick up silicon platelets ($3 \mu\text{m}$ thick, $100 \mu\text{m} \times 100 \mu\text{m}$), which are thinner and lighter than our LEDs ($150 \mu\text{m}$ thick, $100 \mu\text{m} \times 200 \mu\text{m}$).

The pressure of the stamp in the picking up step in Ahmed et al.'s [35] study is 40 mN, which lies in the range of our best picking-up pressure (from 5 to 50 mN). What they pick up are silicon chips ($3 \mu\text{m}$ thick, $250 \mu\text{m} \times 250 \mu\text{m}$), whose size approximately equals our LED sizes ($150 \mu\text{m}$ thick, $100 \mu\text{m} \times 200 \mu\text{m}$).

Yang et al. [37] suggest that the peeling speed should be 15.5 mm/s, while the peeling speed in our study ranges from 17 to 21 mm/s. This means that our stamps are expected to achieve higher transfer printing efficiencies.

4. Conclusions

Via experiments and analyses, we have determined parametric values and criteria that can serve as the guidance for future designs of stamps. For both top and bottom faces, the average error between the post's width and the mold's width can be controlled within 5%. Similarly, the standard deviation of the height of posts fabricated in the same batch can be controlled within $0.5 \mu\text{m}$. The average deviation value between the width of the post and designed mask pattern width stays relatively stable and basically independent of the size. For posts with sizes of $20 \mu\text{m}$ to $180 \mu\text{m}$, the overall average deviation of the top face is positive with the value of $16.84 \mu\text{m}$, whereas that of the bottom face is negative with the value of $-3.23 \mu\text{m}$. During the development process, the photoresist is etched in a semi-ellipsoidal shape. Through fitting, empirical equations regarding r , c , w , and t are obtained. A linear relationship exists between r and c , r and w , as well as c and w , respectively, and the longitudinal etching speed is 1.37 times greater than that in the lateral direction. Fitting results provide a reference for how to realize the fabrication of high-precision posts. Factors that affect the elastic modulus of the stamp are studied, with results showing that the width and the curing temperature play a decisive role in the elastic modulus of the stamp. For posts of the same height, as the width increases, the elastic modulus of the stamp exhibits a maximum value. Finally, for posts of the same size, as the temperature increases, the elastic modulus of the stamp will show two maximum values.

Author Contributions: Conceptualization, W.G.; methodology, C.S.; software, C.S., Y.G., and J.-E.H.; validation, C.S. and H.L.; formal analysis, W.G. and Y.L.; investigation, C.S. and W.G.; resources, Y.L., Y.-J.L., T.W., and Z.C.; data curation, C.S. and W.G.; writing—original draft preparation, C.S.; writing—review and editing, Y.L., T.-M.S., and W.G.; visualization, C.S. and W.G.; supervision, Y.L.; project administration, Z.C.; funding acquisition, Y.L., Y.-J.L., T.W., and Z.C. All authors have read and agreed to the published version of the manuscript.

Funding: This research was funded by the National Natural Science Foundation of China (Grant Nos. 11604285, 51605404, 11904302, and 11674054); the Science and Technology Project of Fujian Province (Grant Nos. 2018H6022, 2019HZ020013, and 2019H6004); the Natural Science Foundation of Fujian Province (Grant No. 2018J01103); the Fundamental Research Funds for the Central Universities (Grant No. 20720190005); and the Strait Postdoctoral Foundation of Fujian Province.

Conflicts of Interest: The authors declare no conflict of interest.

References

1. Katsumi, R.; Ota, Y.; Osada, A.; Yamaguchi, T.; Tajiri, T.; Kakuda, M.; Iwamoto, S.; Akiyama, H.; Arakawa, Y. Quantum-dot single-photon source on a CMOS silicon photonic chip integrated using transfer printing. *APL Photonics* **2019**, *4*, 1–7. [[CrossRef](#)]
2. Shen, L.; Li, H.X.; Meng, X.W.; Li, F. Transfer printing of fully formed microscale InGaP/GaAs/InGaNaSb cell on Ge cell in mechanically-stacked quadruple-junction architecture. *Sol. Energy* **2020**, *195*, 6–13. [[CrossRef](#)]
3. Corbett, B.; Loi, R.; Zhou, W.; Liu, D.; Ma, Z. Transfer print techniques for heterogeneous integration of photonic components. *Prog. Quant. Electron.* **2017**, *52*, 1–17. [[CrossRef](#)]
4. Sheng, X.; Bower, C.A.; Bonafede, S.; Wilson, J.W.; Fisher, B.; Meitl, M.; Yuen, H.; Wang, S.; Shen, L.; Banks, A.R.; et al. Printing-based assembly of quadruple-junction four-terminal microscale solar cells and their use in high-efficiency modules. *Nat. Mater.* **2014**, *13*, 593–598.
5. Corbett, B.; Rodgers, K.; Stam, F.A.; O’Connell, D.; Kelly, P.V.; Crean, G.M. Low-stress hybridisation of emitters, detectors and driver circuitry on a silicon motherboard for optoelectronic interconnect architecture. *Mat. Sci. Semicon. Proc.* **2000**, *3*, 449–453. [[CrossRef](#)]
6. Justice, J.; Bower, C.; Meitl, M.; Mooney, M.B.; Gubbins, M.A.; Corbett, B. Wafer-scale integration of group III-V lasers on silicon using transfer printing of epitaxial layers. *Nat. Photonics* **2012**, *6*, 612–616. [[CrossRef](#)]
7. Bower, C.A.; Menard, E.; Bonafede, S.; Hamer, J.W.; Cok, R.S. Transfer-printed microscale integrated circuits for high performance display backplanes. *IEEE Trans. Compon. Packag. Manuf.* **2011**, *1*, 1916–1922. [[CrossRef](#)]
8. Kim, H.S.; Brueckner, E.; Song, J.Z.; Li, Y.H.; Kim, S.; Lu, C.F.; Sulkin, J.; Choquette, K.; Huang, Y.G.; Nuzzo, R.G.; et al. Unusual strategies for using indium gallium nitride grown on silicon (111) for solid-state lighting. *Proc. Natl. Acad. Sci. USA* **2011**, *108*, 10072–10077. [[CrossRef](#)]
9. Seo, J.H.; Oh, T.Y.; Park, J.; Zhou, W.; Ju, B.K.; Ma, Z. A multifunction heterojunction formed between pentacene and a single-crystal silicon nanomembrane. *Adv. Funct. Mater.* **2013**, *23*, 3398–3403. [[CrossRef](#)]
10. Kim, T.H.; Cho, K.S.; Lee, E.K.; Lee, S.J.; Chae, J.; Kim, J.W.; Kim, D.H.; Kwon, J.Y.; Amaratunga, G.; Lee, S.Y.; et al. Full-colour quantum dot displays fabricated by transfer printing. *Nat. Photonics* **2011**, *5*, 176–182. [[CrossRef](#)]
11. Meitl, M.A.; Zhu, Z.T.; Kumar, V.; Lee, K.J.; Feng, X.; Huang, Y.Y.; Adesida, I.; Nuzzo, R.G.; Rogers, J.A. Transfer printing by kinetic control of adhesion to an elastomeric stamp. *Nat. Mater.* **2006**, *5*, 33–38. [[CrossRef](#)]
12. Gomez, D.; Ghosal, K.; Meitl, M.A.; Bonafede, S.; Prevatte, C.; Moore, T.; Raymond, B.; Kneeburg, D.; Fecioru, A.; Trindade, A.J.; et al. Process capability and elastomer stamp lifetime in micro transfer printing. In Proceedings of the IEEE 66th Electronic Components and Technology Conference (ECTC), Las Vegas, NV, USA, 31 May–3 June 2016; IEEE Computer Soc.: Los Alamitos, CA, USA, 2016.
13. Bower, C.; Meitl, M.; Bonafede, S.; Gomez, D.; Fecioru, A.; Kneeburg, D. Heterogeneous integration of microscale compound semiconductor devices by micro-transfer-printing. In Proceedings of the IEEE 65th Electronic Components and Technology Conference (ECTC), San Diego, CA, USA, 26–29 May 2015; IEEE: New York, NY, USA, 2015.
14. Yoon, J.; Lee, S.; Kang, D.; Meitl, M.; Bower, C.; Rogers, J. Heterogeneously integrated optoelectronic devices enabled by micro-transfer printing. *Adv. Opt. Mater.* **2015**, *3*, 1313–1335. [[CrossRef](#)]
15. Li, R.; Li, Y.; Lu, C.; Song, J.; Saeidpouraza, R.; Fang, B.; Zhong, Y.; Ferreira, P.M.; Rogers, J.A.; Huang, Y. Thermo-mechanical modeling of laser-driven non-contact transfer printing: Two-dimensional analysis. *Soft Matter* **2012**, *8*, 12134. [[CrossRef](#)]
16. Nam, J.; Lee, Y.; Choi, W.; Kim, C.S.; Kim, H.; Kim, J.; Kim, D.H.; Jo, S. Transfer printed flexible and stretchable thin film solar cells using a water-soluble sacrificial layer. *Adv. Energy Mater.* **2016**, *6*, 1–8. [[CrossRef](#)]
17. Bao, C.; Wang, Z.; Liu, Y.; Zhang, Y.; Nie, H.Y.; Lau, W.M.; Mei, J. Mechanics of surface cross-linked polydimethylsiloxane microstructure used for microcontact transfer printing. *J. Appl. Polymer Sci.* **2017**, *134*, 1–7. [[CrossRef](#)]
18. Kim, S.; Wu, J.; Carlson, A.; Jin, S.H.; Kovalsky, A.; Glass, P.; Liu, Z.; Ahmed, N.; Elgan, S.L.; Chen, W.; et al. Microstructured elastomeric surfaces with reversible adhesion and examples of their use in deterministic assembly by transfer printing. *Proc. Natl. Acad. Sci. USA* **2010**, *107*, 17095–17100. [[CrossRef](#)]

19. Chen, H.; Feng, X.; Huang, Y.; Rogers, J.A. Experiments and viscoelastic analysis of peel test with patterned strips for applications to transfer printing. *J. Mech. Phys. Solids* **2013**, *61*, 1737–1752. [[CrossRef](#)]
20. Carlson, A.; Wang, S.; Elvikis, P.; Ferreira, P.M.; Huang, Y.; Rogers, J. Active, programmable elastomeric surfaces with tunable adhesion for deterministic assembly by transfer printing. *Adv. Funct. Mater.* **2012**, *22*, 4476–4484. [[CrossRef](#)]
21. Saeidpourazar, R.; Li, R.; Li, Y.; Sangid, M.D.; Lu, C.; Huang, Y.; Rogers, J.A.; Ferreira, P.M. Laser-driven micro transfer placement of prefabricated microstructures. *J. Microelectromech. Syst.* **2012**, *21*, 1049–1058. [[CrossRef](#)]
22. Bian, J.; Zhou, L.; Wan, X.; Zhu, C.; Yang, B.; Huang, Y.A. Laser Transfer, Printing, and Assembly Techniques for Flexible Electronics. *Adv. Electron. Mater.* **2019**, *5*, 1–33. [[CrossRef](#)]
23. Eisenhaure, J.D.; Xie, T.; Varghese, S.; Kim, S. Microstructured shape memory polymer surfaces with reversible dry adhesion. *ACS Appl. Mater. Interfaces* **2013**, *5*, 7714–7717. [[CrossRef](#)]
24. Choi, M.; Jang, B.; Lee, W.; Lee, S.; Kim, T.W.; Lee, H.J.; Kim, J.H.; Ahn, J.H. Stretchable displays: Stretchable active matrix inorganic light-emitting diode display enabled by overlay-aligned roll-transfer printing. *Adv. Funct. Mater.* **2017**, *27*, 1–10. [[CrossRef](#)]
25. Sun, L.; Jiang, X.; Zhou, Y. Efficient nonfullerene organic solar cells with active layers fabricated by water transfer printing. *J. Energy Chem.* **2019**, *37*, 220–224. [[CrossRef](#)]
26. Linghu, C.; Zhu, H.; Zhu, J.; Li, C.; Song, J. Mechanics of magnet-controlled transfer printing. *Extreme Mech. Lett.* **2019**, *27*, 76–82. [[CrossRef](#)]
27. Chen, C.J.; Chen, H.C.; Liao, J.H.; Yu, C.J.; Wu, M.C. Fabrication and Characterization of Active-Matrix 960×540 Blue GaN-Based Micro-LED Display. *IEEE J. Quantum Elect.* **2019**, *55*, 1–6. [[CrossRef](#)]
28. Zhang, X.; Li, P.; Zou, X.B.; Jiang, J.M.; Yuen, S.H.; Tang, C.W.; Lau, K.M. Active Matrix Monolithic LED Micro-Display Using GaN-on-Si Epilayers. *IEEE Photonic Technol. Lett.* **2019**, *31*, 865–868. [[CrossRef](#)]
29. Um, J.G.; Jeong, D.Y.; Jung, Y.H.; Moon, J.K.; Jung, Y.H.; Kim, S.; Kim, S.H.; Lee, J.S.; Jang, J. Active-Matrix GaN μ -LED Display Using Oxide Thin-Film Transistor Backplane and Flip Chip LED Bonding. *Adv. Electron. Mater.* **2019**, *5*, 1–8. [[CrossRef](#)]
30. Soh, M.Y.; Ng, W.X.; Teo, T.H.; Selvaraj, S.L.; Peng, L.L.; Disney, D.; Zou, Q.; Yeo, K.S. Design and Characterization of Micro-LED Matrix Display With Heterogeneous Integration of GaN and BCD Technologies. *IEEE Trans. Electron Devices* **2019**, *66*, 4221–4227. [[CrossRef](#)]
31. Geum, D.M.; Kim, S.K.; Kang, C.M.; Moon, S.H.; Kyhm, J.H.; Han, J.H.; Lee, D.S.; Kim, S.H. Strategy toward the fabrication of ultrahigh-resolution micro-LED displays by bonding-interface-engineered vertical stacking and surface passivation. *Nanoscale* **2019**, *11*, 23139–23148. [[CrossRef](#)]
32. Guo, W.L.; Tai, J.P.; Liu, J.P.; Sun, J. Process Optimization of Passive Matrix GaN-Based Micro-LED Arrays for Display Applications. *J. Electron. Mater.* **2019**, *48*, 5195–5201. [[CrossRef](#)]
33. Zhang, J.W.; Lin, C.G.; Wang, L.; Zheng, J.Y.; Peng, Y.L.; Duan, D.X. The influence of elastic modulus on the adhesion of fouling organism to poly(dimethylsiloxane) (PDMS). *Adv. Mater. Res.* **2010**, *152–153*, 1466–1470. [[CrossRef](#)]
34. Lee, S.; Kang, B.; Keum, H.; Ahmed, N.; Rogers, J.A.; Ferreira, P.M.; Kim, S.; Min, B. Heterogeneously assembled metamaterials and metadevices via 3D modular transfer printing. *Sci. Rep.* **2016**, *6*, 27621. [[CrossRef](#)] [[PubMed](#)]
35. Ahmed, N.; Rogers, J.A.; Ferreira, P.M. Microfabricated instrumented composite stamps for transfer printing. *J. Micro Nano-Manuf.* **2015**, *3*, 021007. [[CrossRef](#)]
36. Ahmed, N.; Carlson, A.; Rogers, J.A.; Ferreira, P.M. Automated micro-transfer printing with cantilevered stamps. *J. Manuf. Processes* **2012**, *14*, 90–97. [[CrossRef](#)]
37. Yang, S.Y.; Carlson, A.; Cheng, H.; Yu, Q.; Ahmed, N.; Wu, J.; Kim, S.; Sitti, M.; Ferreira, P.M.; Huang, Y.; et al. Elastomer surfaces with directionally dependent adhesion strength and their use in transfer printing with continuous roll-to-roll applications. *Adv. Mater.* **2012**, *24*, 2117–2122. [[CrossRef](#)]
38. Lee, H.; Koh, D.; Xu, L.; Row, S.; Andreadis, S.T.; Oh, K.W. A simple method for fabrication of microstructures using a PDMS stamp. *Micromachines* **2016**, *7*, 173. [[CrossRef](#)]
39. Filippini, L.; Livingston, P.; Kaspar, O.; Tokarova, V.; Nicolau, D.V. Protein patterning by microcontact printing using pyramidal PDMS stamps. *Biomed. Microdevices* **2016**, *18*, 9.1–9.7. [[CrossRef](#)]

40. Wu, J.D.; Dan, Q.; Liu, S. Effect of viscoelasticity of PDMS on transfer printing. In Proceedings of the 16th International Conference on Electronic Packaging Technology, Changsha, China, 11–14 August 2015; IEEE: New York, NY, USA, 2015.
41. Lu, H.; Guo, W.J.; Su, C.W.; Li, X.L.; Lu, Y.J.; Chen, Z.; Zhu, L.H. Optimization on adhesive stamp mass-transfer of micro-LEDs with support vector machine model. *IEEE J. Electron Devices Soc.* **2020**. [[CrossRef](#)]
42. Choi, M.K.; Yang, J.; Kang, K.; Kim, D.C.; Choi, C.; Park, C.; Kim, S.J.; Chae S.I.; Kim, T.H.; Kim, J.H.; et al. Wearable red-green-blue quantum dot light-emitting diode array using high-resolution intaglio transfer printing. *Nat. Commun.* **2015**, *6*, 7149. [[CrossRef](#)]



© 2020 by the authors. Licensee MDPI, Basel, Switzerland. This article is an open access article distributed under the terms and conditions of the Creative Commons Attribution (CC BY) license (<http://creativecommons.org/licenses/by/4.0/>).